A reference model for airborne wind energy systems for optimization and control

E. C. Malz[a,*], J. Koenemann[b], S. Sieberling[c], S. Gros[d]

[a] *Department of Electrical Engineering, Chalmers University of Technology, Göteborg, Sweden*
[b] *Department of Microsystems Engineering (IMTEK), University of Freiburg, Freiburg, Germany*
[c] *Ampyx Power B.V., The Hague, The Netherlands*
[d] *Department of Engineering Cybernetics, Norwegian University of Science and Technology (NTNU), Trondheim, Norway*

Abstract

Airborne Wind Energy (AWE) is a promising new technology, and attracts a growing academic and industrial attention. Important research efforts have been deployed to develop prototypes in order to test the technology, generate control algorithms and optimize the efficiency of AWE systems. By today, a large set of control and optimization methods is available for AWE systems. However, because no validated reference model is available, there is a lack of benchmark for these methods. In this paper, we provide a reference model for pumping mode AWE systems based on rigid wings. The model describes the flight dynamics of a tethered 6 degrees of freedom (DOF) rigid body aircraft in form of differential-algebraic equations, based on Lagrange dynamics. With the help of least squares fitting the model is assessed using real flight data from the Ampyx Power prototype AP2. The model equations are smooth and have a low symbolic complexity, so as to make the model ideal for optimization and control. The information given in this paper aims at providing AWE researchers with a model that has been validated against flight data and that is well suited for trajectory and power output simulation and optimization.

Keywords: wind energy, airborne wind energy, modeling, validation

1. Introduction

In the recent years Airborne Wind Energy (AWE) has attracted a growing interest as a novel wind power technology. AWE harvests wind energy by means of a tethered aircraft flying in a crosswind pattern creating large lift forces. Compared to traditional wind energy technologies, greater altitude can be reached by AWE systems, hence accessing stronger and steadier winds. Another promising advantage of AWE is the reduction of construction material as AWE requires significantly less structure than wind turbines [1]. The two most promising approaches to AWE are the pumping and drag mode [1]. Drag-mode AWE systems are based on rigid wings with onboard turbines generating electrical energy by fast cross wind flights and transmitting the energy to the

*Corresponding author

Email addresses: `elenama@chalmers.se` (E. C. Malz), `Jonas.Koenemann@imtek.de` (J. Koenemann), `soeren@ampyxpower.com` (S. Sieberling), `sebastien.gros@ntnu.no` (S. Gros)

ground via the tether. Pumping-mode AWE systems generate mechanical energy by reeling out a tethered wing from a winch and retract using a fraction of the produced energy.

There exist several companies building prototypes at different scales of both pumping and drag-mode AWE systems [2–4] and the research in AWE control, power maximization and component optimization is increasing [5]. Currently, the technology has not yet reached a commercial deployment and there are many unknowns regarding its viability, pertaining e.g. power availability throughout the year compared to traditional wind turbines, maintenance costs, reliability, safety, legislation, and cost of production. In order to analyze these and other issues, different models have been proposed and used by the AWE community. There exist models for simulation purposes, which include detailed system dynamics with a high complexity. Other models are designed for optimization, which are simplified appropriately and based on at least twice differentiable functions. The models can be further distinguished by their mathematical formulation and the research focus within AWE. In [6] a benchmark model of a soft wing is presented in polar coordinates for optimization purposes. The focus is on the verification of the controller model, but it is not validated against real data. In [7], different soft wing models are presented and compared. The models are real-time oriented but no focus has been laid on the generated power output. In this paper the focus is on a rigid wing model in pumping mode and an accurate power output computation, which both is not given in previous work.

The proposed model uses a description in Cartesian coordinates [8] as opposed to polar coordinates [9, 10], hence providing a formulation that is easier to handle for numerical optimization tools. Tether models have been proposed for AWE systems in [7, 9, 11]. In the model proposed here, we neglect any tether dynamics and consider the tether as a straight rigid link with a mass and an aerodynamic drag. The wing dynamics are represented by the wing position, the translational and rotational speed, the external forces and the orientation, where the orientation is supported via rotation matrices, as proposed in [8].

A similar model formulation has been used in research [12, 13] and in the industry [11] where it was used for optimizing the starting and landing of an AWE system. However, a validation of this model is not available yet. In this paper, we validate this model as a tool for power optimization using real flight data from the Ampyx Power prototype AP2 [2]. The parameters used in the model are provided by the company, and are obtained by CFD analyses, several different test flights and carefully performed measurements.

The validated model is described in detail in this paper, with the purpose of being reproduced and utilized by other researchers, and hence, presents a reference model for research on AWE power optimization. This paper is structured as follows. Section 2 describes the system dynamics and the aerodynamical model in a detailed way. Section 3 presents the wing prototype AP2 and its components, the aerodynamic coefficient determination and the method of comparing model and measurement data. In section 4 the results are presented and discussed. In the last section the conclusions are drawn.

2. Mathematical model

In this section the model dynamics of an AWE system in pumping mode is presented. The system is in the form of differential algebraic equations (DAEs) [14]. The physical formulation of the dynamics is an index-3 DAE based on Lagrange mechanics [15]. For an efficient application of classical integration methods, an index reduction is performed by time differentiating the constraint

twice. This results in a fully implicit index-1 formulation of the dynamics [14] taking the form

$$\mathbf{0} = \mathbf{f}(\dot{\mathbf{x}}, \mathbf{x}, \mathbf{z}, \mathbf{u}) \tag{1}$$

where $\mathbf{f} : \mathbb{R}^{n_{\dot{x}}} \times \mathbb{R}^{n_x} \times \mathbb{R}^{n_z} \times \mathbb{R}^{n_u} \rightarrow \mathbb{R}^{n_x+n_z}$ and $\mathbf{x} \in \mathbb{R}^{n_x}, \mathbf{z} \in \mathbb{R}^{n_z}$ are respectively differential and algebraic states and $\mathbf{u} \in \mathbb{R}^{n_u}$ the control inputs.

Throughout the paper, if not a function, small case letters define scalars, bold small case letters present vectors and bold large case letters define matrices.

2.1. Reference frames

The system is modeled in Cartesian coordinates as done in [8, 13]. Compared to polar coordinates, as used in [10], the modeling in Cartesian coordinates yields less non-linear and less complex equations.

Two reference frames are defined. A fixed right-handed inertial reference frame $\hat{n}$ placed at the attachment point of the tether to ground, with the basis vectors $[\hat{\mathbf{n}}_\mathrm{x}, \hat{\mathbf{n}}_\mathrm{y}, \hat{\mathbf{n}}_\mathrm{z}]$, where $\hat{\mathbf{n}}_\mathrm{y}$ is aligned with the main wind direction and $\hat{\mathbf{n}}_\mathrm{z}$ is down. A second reference frame $\hat{b}$, labelled body frame, is attached to the wing with its origin at the Center of Mass (CoM). The orthogonal unit basis vectors $[\hat{\mathbf{e}}_\mathrm{x}, \hat{\mathbf{e}}_\mathrm{y}, \hat{\mathbf{e}}_\mathrm{z}]$ of the body frame are defined such that $\hat{\mathbf{e}}_\mathrm{x}$ points forward through the nose, $\hat{\mathbf{e}}_\mathrm{y}$ points along the starboard wing, and $\hat{\mathbf{e}}_z$ points down. The reference frames are visualized in Fig. 1.

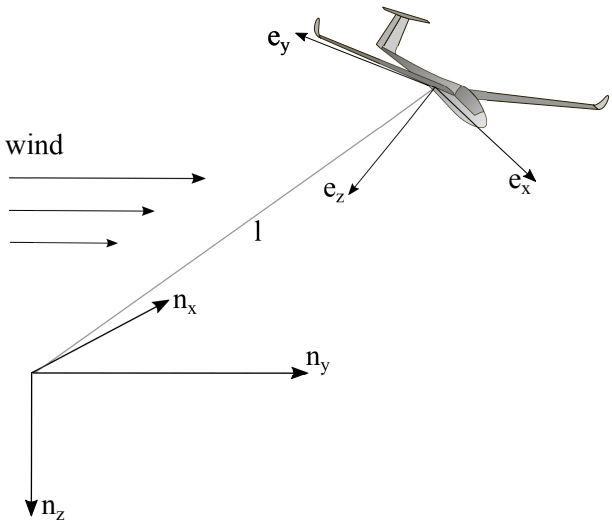

Figure 1: Coordinate system and vector conventions for the rigid-wing AWE system in pumping mode with the tether length l and wind in y direction.

2.2. Model dynamics

The wing is modeled as a one-point mass rigid body with 6 degrees of freedom (DOF) and a straight tether is assumed. The differential and algebraic states as well as control inputs are

$$\mathbf{x} = \begin{bmatrix} \mathbf{p} \\ \mathbf{v} \\ \mathbf{r} \\ \boldsymbol{\omega} \\ l \\ \dot{l} \\ \boldsymbol{\phi} \end{bmatrix} \in \mathbb{R}^{23}, \qquad \mathbf{z} = \lambda \in \mathbb{R} \qquad \mathbf{u} = \begin{bmatrix} \dot{\boldsymbol{\phi}} \\ \ddot{l} \end{bmatrix} \in \mathbb{R}^4, \tag{2}$$

where $\mathbf{p} \in \mathbb{R}^3$ is the CoM position in the inertial frame $\hat{n}$ and $\mathbf{v} \in \mathbb{R}^3$ is the velocity of the CoM in frame $\hat{n}$. Vector $\mathbf{r} \in \mathbb{R}^9$ is a vector representation of matrix $\mathbf{R} \in \mathbb{R}^{3\times 3}$, a direct cosine matrix (DCM), presenting the orientation of the body in earth frame $\hat{n}$. The reason for choosing the DCM representation is two-fold: (i) as the model is aimed at being used within numerical optimal control, it is preferable to use a non-singular representation of the rotations. Indeed, if using a minimal representation (such as e.g. Euler angles), it is difficult to ensure that the model trajectories will not pass through (or close to) the singularity during the iterations performed by the numerical solver. If some iterations come close to the singularity, the solver can fail for purely numerical reasons and hence not deliver a solution of the optimal control problem, (ii) the DCM representation yields models that are less nonlinear than other representations using less states than the DCM. In the context of numerical optimal control, models having less severe nonlinearities are preferred, as they tend to yield a faster and more reliable convergence of the numerical tools deployed for solving the optimal control problem.

Variable $\boldsymbol{\omega} \in \mathbb{R}^3$ is the angular velocity of the wing in frame $\hat{b}$. The variables $l, \dot{l}, \ddot{l} \in \mathbb{R}$ gather the tether components which are the tether length l, speed $\dot{l}$, and the acceleration $\ddot{l}$ as control input. Variables $\boldsymbol{\phi} \in \mathbb{R}^3$, $\dot{\boldsymbol{\phi}} \in \mathbb{R}^3$ collect the control surface deflection aileron $\phi_a \in \mathbb{R}$, elevator $\phi_e \in \mathbb{R}$, and rudder $\phi_r \in \mathbb{R}$ as states and their time derivates as control inputs.

The tether is assumed straight, and is represented in the model by the constraint

$$C = \frac{1}{2}(\mathbf{p}^\top \mathbf{p} - l^2) = 0, \tag{3}$$

stating that the CoM of the wing must be at a distance l of the attachment point of the tether to the ground. Finally, λ is the algebraic variable related to that constraint in Lagrange modeling [15], and is proportional to the tether tension.

Since (3) is *holonomic*, i.e. purely position-dependent, one has to differentiate it twice in order to obtain an index-1 DAE [14], i.e. we use

$$\dot{C} = \mathbf{v}^\top \mathbf{p} - l\dot{l} = 0 \tag{4a}$$

$$\ddot{C} = \dot{\mathbf{v}}^\top \mathbf{p} + \mathbf{v}^\top \mathbf{v} - \dot{l}^2 - l\ddot{l} = 0. \tag{4b}$$

The index reduced DAE then enforces (4b) at all time, and (3)-(4a) at an arbitrary point in time, e.g. $t = 0$.

The evolution of the position and orientation of the wing are then simply expressed as

$$\dot{\mathbf{p}} = \mathbf{v}, \qquad \dot{\mathbf{R}} = \mathbf{R}\omega_{\times}, \tag{5}$$

where $\omega_{\times}$ is the skew symmetric matrix associated to the rotational velocity $\boldsymbol{\omega}$. In order to have a valid DCM $\mathbf{R}$, the orthonormality constraint

$$\mathbf{R}^{\top}\mathbf{R} - \mathbf{I} = 0 \tag{6}$$

must be imposed at an arbitrary point in time, e.g. $t = 0$.

The translational and rotational acceleration of the wing $\dot{\mathbf{v}}, \dot{\boldsymbol{\omega}}$ are defined by the gravitational, tether, aerodynamic forces and moments acting on the wing. All forces act at the CoM of the wing. Gravitation is computed as $\mathbf{F}_{\mathrm{g}} = m \cdot g \cdot \hat{\mathbf{n}}_{\mathrm{z}}$, where m as the mass of the system and $g = 9.81\mathrm{m/s}^2$. The drag and lift forces acting on the wing are combined in a single aerodynamic force $\mathbf{F}_{\mathrm{A}}$. An additional drag $\mathbf{F}_{\mathrm{Tdrag}}$ is created by the tether. The detailed aerodynamic model for computing $\mathbf{F}_{\mathrm{A}}$ and $\mathbf{F}_{\mathrm{Tdrag}}$ is given in the section 2.3. The tether force acting on the wing reads as

$$\mathbf{F}_{\mathrm{t}} = \lambda \mathbf{p}. \tag{7}$$

The sum of the forces yields the wing acceleration, i.e.

$$\dot{\mathbf{v}} = m^{-1}\left[\mathbf{F}_{\mathrm{A}} + \mathbf{F}_{\mathrm{g}} + \mathbf{F}_{\mathrm{T}drag} + \mathbf{F}_{\mathrm{t}}\right]. \tag{8}$$

The rotational acceleration $\dot{\boldsymbol{\omega}}$ is purely related to the aerodynamic moments $\mathbf{M}_{\mathrm{A}}$ and reads as:

$$\dot{\boldsymbol{\omega}} = \mathbf{J}^{-1}\left[\mathbf{M}_{\mathrm{A}} - (\boldsymbol{\omega} \times \mathbf{J} \cdot \boldsymbol{\omega})\right], \tag{9}$$

where $\mathbf{J}$ is the inertia matrix of the wing in the body frame. The detailed computation of the aerodynamic moments $\mathbf{M}_{\mathrm{A}}$ is explained in section 2.3.

Equations (4b), (5),(8), (9) result in the full system dynamics. The addition of the constraints of $(4a)|_{\mathrm{t}=0}, (3)|_{\mathrm{t}=0}$ and $(6)|_{\mathrm{t}=0}$ complete the dynamics of the AWE system. When implementing this model in a power optimization problem, where a periodic optimization is solved, additional care has to be taken in formulating and solving the problem, which is detailed in [13, 16, 17]. The next section gives a detailed explanation of the aerodynamic model.

2.3. Aerodynamic model

The aerodynamic model contains the computation of the aerodynamic forces and moments, which are nonlinear functions of the system states. The aerodynamic forces and moments interact with the kinematics in a feedback fashion, as the forces and moments depend on the states and influence their time evolution. This feedback loop makes the model dynamics highly complex and unstable. The aerodynamics are similar to standard aircraft flight mechanics, but the presence of the tether yields drastically different dynamics.

The wind acting on the system is given in the earth coordinate frame $\hat{n}$. The wind is commonly approximated via the power law wind shear model [18], in which the wind has a constant direction and its speed is a function of the altitude $h = -\mathbf{p}_3$. It is given by

$$\|\mathbf{w}\| = w_0 \left(-\frac{\mathbf{p}_3}{h_0}\right)^{z}, \tag{10}$$

where h_0 is a wind shear reference altitude, w_0 the wind magnitude at that reference altitude, and z a roughness coefficient representing the shear effect. Note, that $\mathbf{w} = [w_x, w_y, w_z]$ is a 3-dimensional vector and can hold also varying winds or wind profiles if a more detailed wind model is desired. Using wind $\mathbf{w}$ the apparent velocity of the wing is given by

$$\mathbf{v}_\mathrm{a} = \mathbf{v} - \mathbf{w} \tag{11}$$

in frame $\hat{n}$. It describes the actual wind flow the wing experiences during flight. The forces acting on the wing dependent on the apparent speed are described in the earth frame $\hat{n}$ as:

$$\mathbf{F}_\mathrm{A} = \frac{1}{2}\,\rho\,\|\mathbf{v}_\mathrm{a}\|^2 S\,\mathbf{R}\begin{bmatrix} C_\mathrm{X} \\ C_\mathrm{Y} \\ C_\mathrm{Z} \end{bmatrix}, \tag{12}$$

where S is the aerodynamic reference area corresponding to the projected surface area of the wing, and ρ is the local air density.

The aerodynamic moment with coefficients C_l, C_m C_n is defined similarly, though it is common to express it in the body frame. It reads as:

$$\mathbf{M}_\mathrm{A} = \frac{1}{2}\,\rho\,\|\mathbf{v}_\mathrm{a}\|^2 S\begin{bmatrix} b\,C_\mathrm{l} \\ c\,C_\mathrm{m} \\ b\,C_\mathrm{n} \end{bmatrix}, \tag{13}$$

where b is the reference wingspan and c is the reference chord length of the wing. This aerodynamic model is based on the assumption that the airflow around the wing settles instantaneously to its steady-state, such that the aerodynamic forces and moments depend on the instantaneous state $\mathbf{x}$ of the airframe only.

The airflow direction is defined by the aerodynamic angle of attack α and sideslip angle β which are expressed in radians in the body frame as:

$$\alpha = \arctan\left(\frac{\hat{\mathbf{e}}_\mathrm{z}^\top \mathbf{v}_\mathrm{a}}{\hat{\mathbf{e}}_\mathrm{x}^\top \mathbf{v}_\mathrm{a}}\right), \qquad \beta = \frac{\hat{\mathbf{e}}_\mathrm{y}^\top \mathbf{v}_\mathrm{a}}{\hat{\mathbf{e}}_\mathrm{x}^\top \mathbf{v}_\mathrm{a}}. \tag{14}$$

These angles, together with the surface deflections $\boldsymbol{\phi}$, are needed in order to compute the corresponding aerodynamic coefficients $C_{\{\mathrm{X,Y,Z}\}}, C_{\{\mathrm{l,m,n}\}}$ given by

$$\begin{aligned}\begin{bmatrix} C_X \\ C_Y \\ C_Z \end{bmatrix} &= \begin{bmatrix} C_{X0}(\alpha) \\ C_{Y0}(\alpha) \\ C_{Z0}(\alpha) \end{bmatrix} + \begin{bmatrix} C_{X\beta}(\alpha) \\ C_{Y\beta}(\alpha) \\ C_{Z\beta}(\alpha) \end{bmatrix}\beta \\ &+ \begin{bmatrix} C_{Xp}(\alpha) & C_{Xq}(\alpha) & C_{Xr}(\alpha) \\ C_{Yp}(\alpha) & C_{Yq}(\alpha) & C_{Yr}(\alpha) \\ C_{Zp}(\alpha) & C_{Zq}(\alpha) & C_{Zr}(\alpha) \end{bmatrix}\begin{bmatrix} b\,\omega_x \\ c\,\omega_y \\ b\,\omega_z \end{bmatrix}\frac{1}{2\|\mathbf{v}_\mathrm{a}\|} \\ &+ \sum_{i\in\{a,e,r\}}\begin{bmatrix} C_{X\phi_i}(\alpha)\,\phi_i \\ C_{Y\phi_i}(\alpha)\,\phi_i \\ C_{Z\phi_i}(\alpha)\,\phi_i \end{bmatrix},\end{aligned} \tag{15}$$

and

$$\begin{aligned}\begin{bmatrix} C_l \\ C_m \\ C_n \end{bmatrix} &= \begin{bmatrix} C_{l0}(\alpha) \\ C_{m0}(\alpha) \\ C_{n0}(\alpha) \end{bmatrix} + \begin{bmatrix} C_{l\beta}(\alpha) \\ C_{m\beta}(\alpha) \\ C_{n\beta}(\alpha) \end{bmatrix} \beta \\ &+ \begin{bmatrix} C_{lp}(\alpha) & C_{lq}(\alpha) & C_{lr}(\alpha) \\ C_{mp}(\alpha) & C_{mq}(\alpha) & C_{mr}(\alpha) \\ C_{np}(\alpha) & C_{nq}(\alpha) & C_{nr}(\alpha) \end{bmatrix} \begin{bmatrix} b\,\omega_x \\ c\,\omega_y \\ b\ \omega_z \end{bmatrix} \frac{1}{2\|\mathbf{v}_\mathrm{a}\|} \\ &+ \sum_{i\in\{a,e,r\}} \begin{bmatrix} C_{l\phi_i}(\alpha)\,\phi_i \\ C_{m\phi_i}(\alpha)\,\phi_i \\ C_{n\phi_i}(\alpha)\,\phi_i. \end{bmatrix}\end{aligned} \tag{16}$$

The aerodynamic coefficients $C_{\{\mathrm{X,Y,Z}\}}, C_{\{\mathrm{l,m,n}\}}$ are generally estimated via flight tests and presented as look-up tables in terms of the angle of attack α, the side slip β, and the surface controls $\boldsymbol{\phi}$. For modeling and optimization purposes these look-up tables need to be approximated by e.g. polynomials or spline functions. Such method is sufficiently accurate for attached flows at low angles of attack. In this paper the coefficients for the Ampyx wing AP2 are used, listed in Section 3.1.

One of the main differences between a conventional and a tethered wing is the presence of the tether which induces additional drag, weight and possibly moments if the tether is not attached at the CoM of the wing. A model of the tether is crucial for an accurate AWE model. In this model it is assumed that the tether is attached at the CoM of the wing, such that drag does not generate moments in the wing dynamics. In [19] the drag force generated by the whole tether length is simplified in to

$$T_\mathrm{D} = \frac{1}{8}\,\rho\,C_\mathrm{T}\,d_\mathrm{tet}\,l\,\|\mathbf{v}_\mathrm{a}\|, \tag{17}$$

where C_T is the drag coefficient and d_tet the tether diameter. It is assumed that the drag is acting on the wing in the direction $\mathbf{v}_\mathrm{a}$, which results in the tether drag, described in earth frame,

$$\mathbf{F}_\mathrm{Tdrag} = -T_\mathrm{D}\mathbf{v}_\mathrm{a}. \tag{18}$$

Dynamics and constraints can be adjusted in order to include a refined tether model or adding e.g. a ground station representing the mechanical-electrical energy conversion.

3. Method

In this section, we present the Ampyx Power prototype (AP2) and the procedure deployed for obtaining the wing parameters and the real test flight data. We then explain the procedure of assessing the capability of the model to match the flight data.

3.1. Description of the AWE prototype

The Ampyx Power Prototype 2 (AP2) AWE system is a prototype built by the dutch company Ampyx Power B.V. in order to develop and test new control algorithms for AWE and push the technology towards its full automation [2]. First flown in 2009, the 30 kW system with 5.5 m wingspan comprises several years of development and technological progress and is, by the time of writing, one of the most advanced airborne wind energy systems in the world. The AP2 wing is displayed in Fig. 2. Because of the availability of data and parameters, and the willingness of the company to share flight information, this system is used in this work.

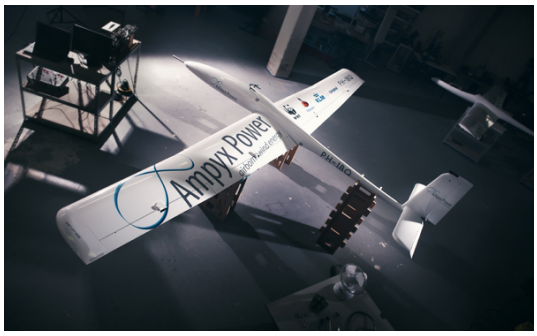

Figure 2: Ampyx Power prototype AP2 [2]. The flight data were collected during several test flights with this prototype.

3.1.1. Physical components of the system

The AP2 system consists of a ground-based generator, a winch, a polyethylene tether, and a wing that also contains electrical components for the automatic control of the flight. Because the focus is laid on the validation of the flight model and the mechanical power output, the electrical details of the generator are omitted. The wing is controlled using classical control surfaces i.e. a rudder at the vertical stabilizer for yaw control, elevators at the horizontal stabilizer for pitch control, and ailerons at the wing for rolling maneuvers. The deflection of the control surfaces are measured and collected in vector $\hat{\boldsymbol{\phi}} \in \mathbb{R}^3$. Flaps are only active during landing and are therefore not considered here.

The prototype is equipped with several sensors, installed in the winch and on the wing. The wing is equipped with a GPS sensor, IMU sensor, and a pitot tube. Using filter algorithms, this sensor information is fused to estimate the position $\hat{\mathbf{p}} \in \mathbb{R}^3$, velocity $\hat{\mathbf{v}} \in \mathbb{R}^3$, orientation $\hat{\mathbf{R}} \in \mathbb{R}^{3\times 3}$, the rotational speed $\hat{\boldsymbol{\omega}} \in \mathbb{R}^3$, airspeed $\hat{\mathbf{v}}_\mathrm{A} \in \mathbb{R}^3$, the angle of attack $\hat{\alpha} \in \mathbb{R}$ and the angle of sideslip $\hat{\beta} \in \mathbb{R}$. The horizontal wind speed $\hat{\mathbf{w}} \in \mathbb{R}^2$ is estimated based on signals obtained from a 5-holes probe and the GPS velocity. At the winch the tether speed $\hat{\dot{l}} \in \mathbb{R}$, tether acceleration $\hat{\ddot{l}} \in \mathbb{R}$, and tether force $\hat{\mathbf{F}}_\mathrm{t} = \lambda\|\mathbf{p}\| \in \mathbb{R}$ are estimated. This data are logged at a frequency of 50 Hz during each flight.

The flight model described in Section 2 depends on parameters that are specific for this prototype. The kinematic and geometric parameters are summarized in Table 1. The aerodynamic parameters are described in the next subsection.

3.1.2. Determination of the aerodynamic coefficients

The aerodynamic coefficients of the wing have been identified by Ampyx Power with the help of CFD analyses in AVL [20] and during several untethered test flights. During these flights short maneuvers were flown in which specific control inputs were given and the responses of the system were recorded. For each control surface, separate untethered test flights were executed to determine the aerodynamic coefficients individually whenever possible. The resulting coefficients C_XYZ and C_lmn for the aerodynamic forces and moments have then been represented as polynomial functions of the angle of attack α. In Table 2 the polynomial coefficients are listed as $[c_2\, c_1\, c_0]$ such that the

Table 1: Kinematic and geometric system specifications of Ampyx wing AP2

parameter	value	description
S	3	wing area [m^2]
b	5.5	wing span [m]
c	0.55	wing chord [m]
m	36.8	weight [kg]
$J_{(\mathrm{xx,yy,zz,xz})}$	25, 32, 56, -0.47	inertia matrix [kg·m^2]
d_{tet}	0.0025	tether diameter [m]
ρ_{t}	0.0046	tether density [kg/m]
C_{t}	1.2	tether drag coefficient [-]
ρ	1.225	air density [kg/m^3]

aerodynamic coefficients are obtained as

$$C_{.} = \begin{bmatrix} c_2 & c_1 & c_0 \end{bmatrix} \begin{bmatrix} \alpha^2 \\ \alpha \\ 1 \end{bmatrix}. \tag{19}$$

Parameters that are not listed are equal to zero.

Table 2: Dimensionless polynomial coefficients resulting in the aerodynamic coefficients which are implemented in the aerodynamic model (15) and (16), using convention (19).

C_X	value	C_m	value
C_{X_0}	[2.5549, 0.4784, -0.0293]	C_{m_0}	[0,-0.6027, -0.0307]
C_{X_q}	[0, 4.4124, -0.6029]	C_{m_q}	[5.2885,-0.0026,-11.3022]
$C_{X_{\phi_e}}$	[0, 0.1115,-0.0106]	$C_{m_{\phi_e}}$	[0.9974,-0.0061,-1.0427]
		$C_{m_{\phi_r}}$	[0,0,-0.0015]
C_Y		C_l	
C_{Y_β}	[0.0936,-0.0299,-0.1855]	C_{l_β}	[0.0312,-0.0003 ,-0.0630]
C_{Y_p}	[0.0496,-0.0140,-0.1022]	C_{l_p}	[0.2813,-0.0247,-0.5632]
C_{Y_r}	[0,0.1368,0.1694]	C_{l_r}	[0,0.6448,0.1811]
$C_{Y_{\phi_a}}$	[0.0579,-0.0024,-0.0514]	$C_{l_{\phi_a}}$	[0.2383,-0.0087,-0.2489]
$C_{Y_{\phi_r}}$	[-0.1036,0.0268,0.10325]	$C_{l_{\phi_r}}$	[0,-0.0013,0.00436]
C_Z		C_n	
C_{Z_0}	[5.7736, -5.0676, -0.5526]	C_{n_β}	[0,-0.0849,0.0577]
C_{Z_q}	[6.1486,0.1251,-7.5560]	C_{n_p}	[0,-0.9137,-0.0565]
$C_{Z_{\phi_e}}$	[0.2923,-0.0013,-0.315]	C_{n_r}	[0.02570,0.0290,-0.0553]
		$C_{n_{\phi_a}}$	[0,-0.1147,0.01903]
		$C_{n_{\phi_r}}$	[0.04089,-0.0117,-0.0404]

3.2. Formulation of the validation problem

It is important to observe here that while physical parameters such as masses, inertias, lengths and diameters are comparably easy to estimate accurately, the parameters underlying the aerodynamic model are, in contrast, more difficult to estimate.

We propose to assess the model on the real data via performing a fitting of the model trajectories to the measurements obtained during real flight experiments, i.e. a least squares problem

minimizing the difference between model and measurement data. This approach will allow us to observe what parts of the model trajectories cannot accurately fit the real data, and identify what parts of the model are the least accurate. The measurements to be fitted to the model are collected in the data output vector $\hat{\mathbf{y}} = [\hat{\mathbf{p}}, \hat{\mathbf{v}}, \hat{\mathbf{R}}, \hat{\boldsymbol{\omega}}, \hat{\dot{l}}, \hat{\mathbf{w}}, \hat{\phi}]$ and the corresponding model output in $\mathbf{y} = [\mathbf{p}, \mathbf{v}, \mathbf{R}, \boldsymbol{\omega}, \dot{l}, \mathbf{w}, \phi]$.

For the validation the wind speed $\mathbf{w}$ is not modeled by the wind shear model (10), but the state $\mathbf{w} \in \mathbb{R}^2$ is introduced in the model, following the dynamics:

$$\dot{\mathbf{w}} = \mathbf{u}_{\mathbf{w}} \tag{20}$$

and $\mathbf{w}$ is fitted to the wind data while $\mathbf{u}_{\mathbf{w}}$ is minimized using a square penalty. We therefore assume that the wind can be described as a random walk driven by a Gaussian white noise.

The fitting problem minimizing the difference between measurement data and model can be formulated as

$$\begin{aligned} \min_{\mathbf{y}} \quad & \int_0^{t_f} (\mathbf{y} - \hat{\mathbf{y}})^\top W_{\mathbf{y}} (\mathbf{y} - \hat{\mathbf{y}}) + W_{\mathbf{w}} \|\mathbf{u}_{\mathbf{w}}\|^2 \, \mathrm{d}t \\ \text{s.t.} \quad & (4\text{b}), (5), (8), (9), (3)|_{\text{t}=0}, (4\text{a})|_{\text{t}=0}, (6)|_{\text{t}=0}, (20) \end{aligned} \tag{21}$$

The cost function in (21) penalizes the differences between the model output $\mathbf{y}$ and measured data $\hat{\mathbf{y}}$. Matrix $\mathbf{W}_{\mathbf{y}}$ and scalar $W_{\mathbf{w}}$ should ideally hold the inverse of the covariance matrix of the measurement noises and wind rate of change. As this information is difficult to obtain, reasonable ad hoc values are chosen instead.

Problem (21) is solved numerically using the *direct collocation* method, which belongs to the family of direct optimal control methods [21]. The problem is discretized into a finite-dimensional NLP by splitting the state trajectories into 60 control intervals. Within each control interval the trajectories are represented by a Lagrange polynomial evaluated on the collocation points using a Radau scheme of degree 3 [22]. The Radau scheme is chosen due to its good numerical stability at the presence of DAEs [21, 22].

4. Results

In the previous section we described the method and tools we use in order to assess the model of the AWE system. In this section, the results of the fitting problem are shown and discussed.

4.1. Validation results

The method explained in Section 3 was used to assess the proposed model. The measurement data correspond to one pumping cycle that spans 50 s. One pumping cycle includes the reel-out of a single phase and the subsequent retraction phase. Several sequences of pumping cycles at different time points were extracted from the data for the validation procedure, resulting all in similar results. For the presentation of the results one cycle was selected.

The flight path during the actually flown power cycle is presented in Fig. 3.

The trajectory does not end exactly at the same position as the starting position because the flight controller does not enforce periodicity and the subsequent power orbit is slightly shifted. The small wings visualize the direction of flight and the red segments visualize the reel-in phase of the tether. The main wind direction is displayed as blue arrows in the plot.

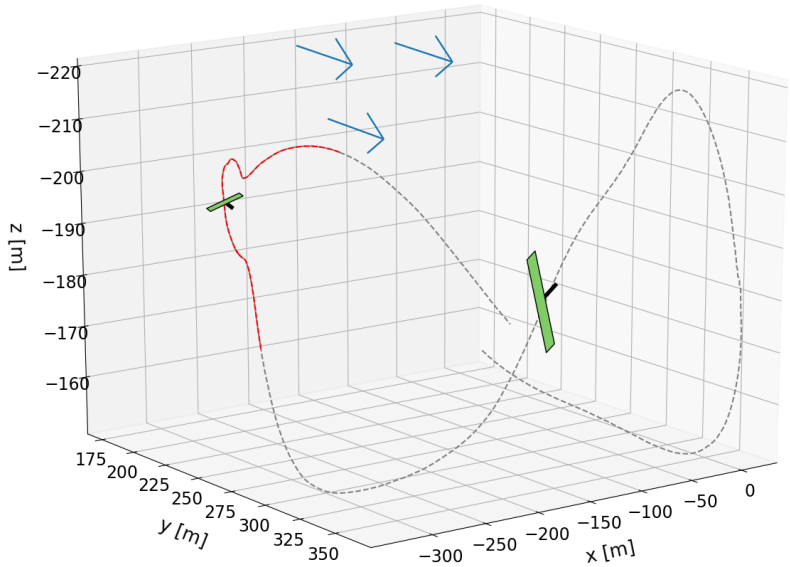

Figure 3: 3D plot of the fitted flight path of one pumping cycle, with the black small rod marking the tail of the wing. Red marked part defines the reel-in phase of the tether. The blue arrows label the wind direction.

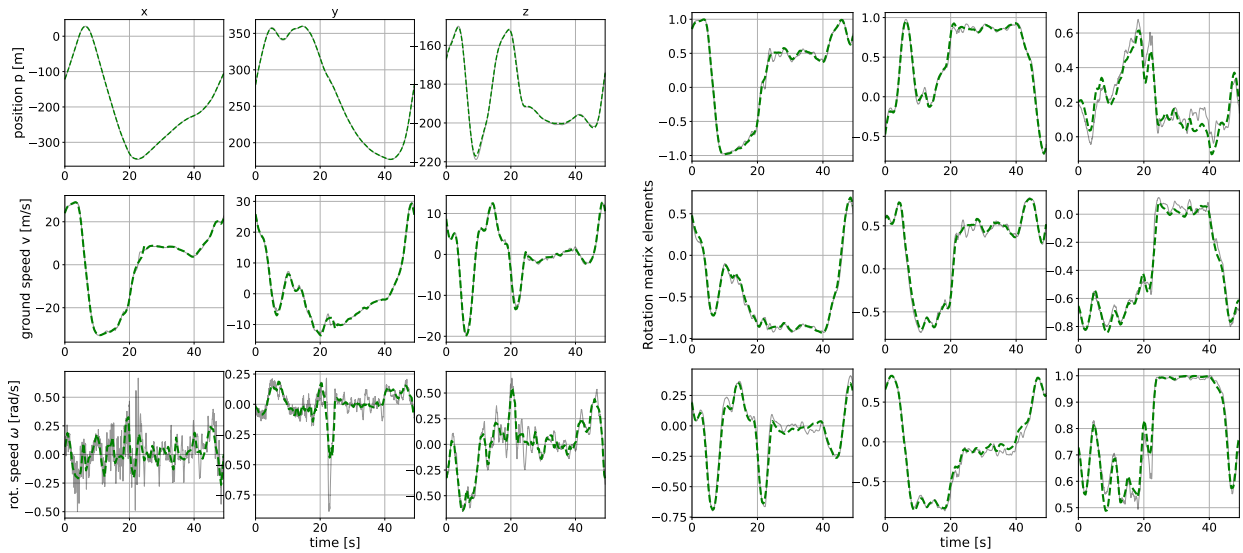

Figure 4: Left: Position $\mathbf{p}$ [m], speed $\mathbf{v}$ [m/s], angular velocity $\boldsymbol{\omega}$ [rad/s]. Right: rotation matrix $\mathbf{R}$. For both the data (solid grey) and model (dashed green) are shown. For all variables the model presents a good fit to the data.

Fig. 4 presents the position $\mathbf{p}$, ground speed $\mathbf{v}$ and rotational speed $\boldsymbol{\omega}$ in the body frame on the left and the rotation matrix $\mathbf{R}$ on the right.

The data is colored in solid grey, whereas the modeled variables are displayed in dashed green. The same color code is used throughout the whole result section. The plots in Fig. 4 present a good fit for all the variables. The measurements $\hat{\boldsymbol{\omega}}$ are noisy, while the trajectories of the modeled $\boldsymbol{\omega}$ are smoother compared to the data but follow the trend. The wind speed in the model and the

original wind speed data is plotted in Fig. 5. The measurements contain only the horizontal wind components. It can be observed that due to the introduction of $\mathbf{u_w}$ the wind trajectory, which is fed to the aerodynamic model is smoother than the actual measurement data. Variables $\|\mathbf{v}_\mathrm{a}\|$,

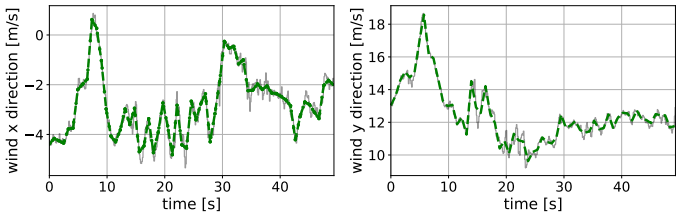

Figure 5: Wind variable $\mathbf{w}$ fitted to wind measurements. Data in solid grey, model in dashed green.

α and β are displayed in Fig. 6. A mismatch between data and model of α and β is visible, but

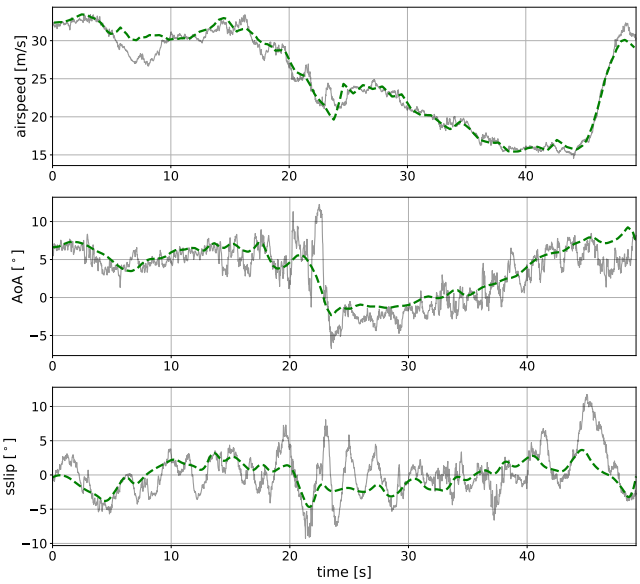

Figure 6: Apparent speed $||\mathbf{v}_\mathrm{a}||$[m/s], the angle of attack α[°] and the side slip β[°] follow the trend of the data. Measurement data in solid grey, model in dashed green. The aerodynamic angles are generally difficult to measure which is probably the reason for the slight mismatch. However, the general trend is adequate.

the general trend is adequate. The aerodynamic angles are generally difficult to measure which makes a mismatch likely. In Fig. 7 the surface deflections $\boldsymbol{\phi}$, aileron, elevator and rudder are displayed. One can observe an oscillation in the aileron in the first half of the data which does not appear the model. The modeled surface deflections are in general smoother than the data, but the trend of the trajectories fits well. In general, the model appears capable of fitting real tethered flight data regarding all variables including position, speed, rotation, angular velocities, aerodynamic angles, apparent speed and the surface deflections. From these results we conclude that kinematic, geometric, aerodynamic and lift and drag models are a fair representation of the real system dynamics. In the next section, we assess the capability of the model at predicting the mechanical power extracted by the system.

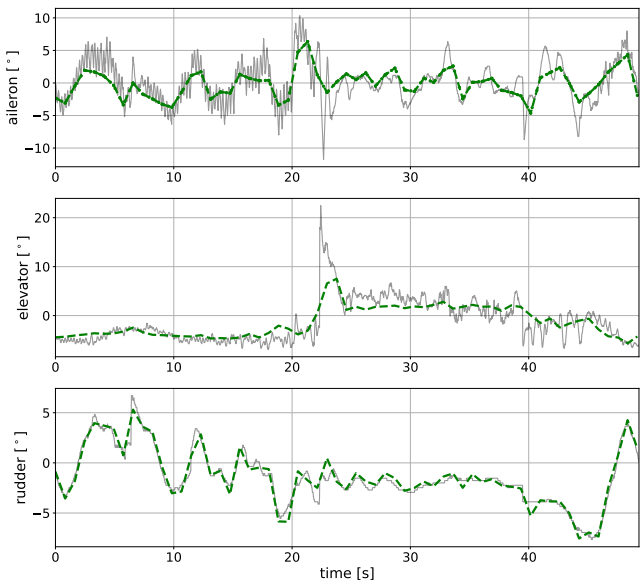

Figure 7: Control surface deflections $\phi[°]$ (aileron, elevator and rudder). Measurement data in solid grey, model in dashed green. The trajectory of the modeled surface deflections is smoother but follows the trend of the data.

4.2. Power output

The power output of the system is mainly defined by the tether speed and tether tension. Fig. 8 (top) displays the tether reel-in and reel-out speed, both from the model and the measurements. The reel-out phase ($\dot{l} > 0$) generates power while the reel-in phase ($\dot{l} < 0$) consumes power. Fig. 8 (top) shows a better fit of the tether speed during the reel-out phase than during the reel-in. The difference in fit might be due to the straight tether assumption in the model. Indeed, during the traction phase the tether is under high tension, i.e. the straight tether assumption in the model is fair. However, under lower tension, during the retraction phase, the tether is likely to sag more, resulting in a larger mismatch. The measured and modeled tether tension is displayed in Fig. 8 (bottom). The modeled tether tension is given by $\lambda\|\mathbf{p}\|$. During the high-tension phase, severe oscillations can be seen in the measurements, which are most likely caused by real tether oscillations. As the model does not incorporate tether elasticity, it can not capture such oscillations. In general the tether tension estimated by the model follows nonetheless decently well the average measured tension.

The good match is a quite striking observation provided that a simple straight tether model was used in this work. Hence, in the context of assessing power generation, the straight tether assumption appears justified.

The mechanical power output is computed in the model as $P_{mech} = \lambda \cdot ||\mathbf{p}|| \cdot \dot{l}$. In Fig. 9 the power output over the orbit is displayed. The actual mechanical power output is estimated by multiplying the measured tether speed and tether tension. The power needed to reel in the aircraft is a small fraction of the mechanical power extracted at the reel-out phase. The total energy production over this pumping cycle is computed as the integral over the instantaneous power output. In the data the energy of one cycle is 66.52 Wh whereas the model estimates the energy to 65.91 Wh. The relative error is calculated as 0.92%.

This observation suggests that the tether oscillations observed in Fig. 8 do not dissipate a sig-

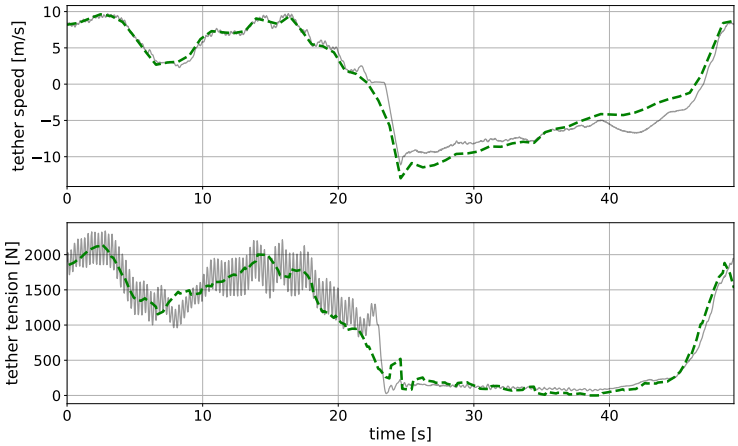

Figure 8: Top: tether speed (winch reel-in/-out speed) $[m/s]$. Bottom: tether tension in [N]. Measurement data in solid grey and model in dashed green. The visible oscillations in the measurements are most likely tether oscillations, which are however not captured in the model.

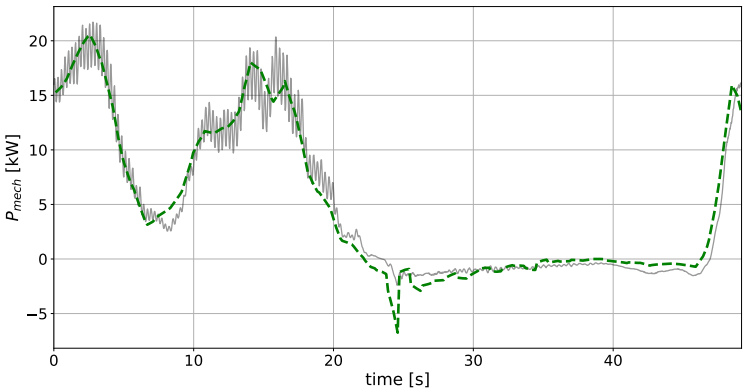

Figure 9: Mechanical power output $[W]$ of one pumping cycle. Measurement data in solid grey and model in dashed green.

nificant amount of energy, allowing the very good fit in the energy of the cycle under investigation. Hence, we assume that the tether oscillations are longitudinal in this prototype, and do not require the correction of an increased tether drag discussed in [23]. However, tether oscillations as the ones measured here arguably have a strong impact on component fatigue, and ought to be accounted for at the mechanical design phase.

The model was tested against multiple data sets and showed for all similarly good results. The different data sets were collected during a stable flight session at average wind conditions. For a more general assessment of the model, data should be collected during flights at low and high wind speeds and tested against the model. This limits the validity of the proposed model to power production cycles during average wind conditions.

5. Conclusion

In this paper a reference model of an airborne wind energy system in pumping mode was detailed and validated against real flight data of the a prototype wing AP2 of Ampyx Power. The validation was performed via a least squares fitting problem of the model state trajectories to complete flight data (position, speed, rotation, angular velocity, apparent wind speed and aerodynamic angles). The time horizon of the fitting was a single pumping cycle of 50s, comprising a reel-out and reel-in phase. The observations drawn on fitting this pumping cycle appeared consistent throughout the pumping cycles available in the dataset. It appears that the proposed model is capable of explaining very well the data obtained in the real system. The proposed model appeared fairly accurate at predicting the average power output of the system.

The tether speed and resulting mechanical power output are very close fit to the measurement with a relative error in output power of 0.92% . The tether tension of the model fits the data fairly well with some mismatch at specific times. Thus, we conclude that the assumption of a straight tether is an appropriate model choice in the context of power generation estimation. Despite the assumptions and simplifications proposed, the model presented is capable of explaining the real data obtained in the AWE prototype developed by Ampyx Power and thus presents a valid reference model for research related to power generation within AWE at average wind conditions. Future work ought to test the model for flights during more extreme wind conditions in order to assess its general validity.

Acknowledgment

This work is supported by the project AWESCO (H2020-ITN-642682) funded by the European Union's Horizon 2020 research and innovation program under the Marie Skłodowska-Curie grant agreement No 642682.

References

[1] A. Cherubini, A. Papini, R. Vertechy, and M. Fontana, "Airborne wind energy systems: A review of the technologies," *Renewable and Sustainable Energy Reviews*, vol. 51, pp. 1461 – 1476, 2015.

[2] *Ampyx Power*, Available at https://www.ampyxpower.com, 2017.

[3] *Makani*, Available at https://x.company/makani/, 2019.

[4] *Twintec*, Available at http://twingtec.ch, 2018.

[5] *AWESCO*, Available at http://awesco.eu.

[6] S. Costello, G. François, and D. Bonvin, "Crosswind kite control – a benchmark problem for advanced control and dynamic optimization," *European Journal of Control*, vol. 35, pp. 1 – 10, 2017.

[7] U. Fechner, R. van der Vlugt, E. Schreuder, and R. Schmehl, "Dynamic model of a pumping kite power system," *Renewable Energy*, vol. 83, pp. 705–716, 2015.

[8] S. Gros and M. Diehl, *Modeling of Airborne Wind Energy Systems in Natural Coordinates*. Berlin, Heidelberg: Springer Berlin Heidelberg, 2013, pp. 181–203.

[9] P. Williams, B. Lansdorp, and W. Ockels, "Modeling and control of a kite on a variable length flexible inelastic tether," vol. 2, 08 2007.

[10] L. Fagiano, M. Milanese, and D. D. Piga, "Optimization of airborne wind energy generators," *International Journal of Robust and Nonlinear Control*, vol. 22, no. 18, pp. 2055–2083, 2012.

[11] J. Koenemann, P. Williams, S. Sieberling, and M. Diehl, "Modeling of an airborne wind energy system with a flexible tether model for the optimization of landing trajectories," *IFAC-PapersOnLine*, vol. 50, no. 1, pp. 11 944 – 11 950, 2017, 20th IFAC World Congress.

[12] G. Licitra, J. Koenemann, P. Williams, R. Ruiterkamp, G. Horn, and M. Diehl, "Viability assessment of a rigid wing airborne wind energy pumping system." in *Proceedings of the 2017 21st International Conference on Process Control, PC 2017*, no. Proceedings of the 2017 21st International Conference on Process Control, PC 2017, Ampyx Power B.V, 2017, pp. 452–458.

[13] G. Horn, S. Gros, and M. Diehl, *Numerical Trajectory Optimization for Airborne Wind Energy Systems Described by High Fidelity Aircraft Models.* Berlin, Heidelberg: Springer Berlin Heidelberg, 2013, pp. 205–218.

[14] U. M. Ascher and L. R. Petzold, *Computer methods for ordinary differential equations and differential-algebraic equations.* Philadelphia: Society for Industrial and Applied Mathematics, 1998.

[15] A. J. Brizard, *An introduction to Lagrangian Mechanics.* World Scientific, 2015.

[16] S. Gros and M. Zanon, "Numerical optimal control with periodicity constraints in the presence of invariants," *IEEE Transactions on Automatic Control*, vol. 63, no. 9, pp. 2818–2832, 2017.

[17] S. Gros, M. Zanon, and M. Diehl, "A relaxation strategy for the optimization of airborne wind energy systems," in *2013 European Control Conference (ECC)*, July 2013, pp. 1011–1016.

[18] L. Landberg, *Meteorology for wind energy: an introduction*, 1st ed. Wiley, 2016.

[19] I. Argatov and S. Risto, *Efficiency of Traction Power Conversion Based on Crosswind Motion.* Springer Berlin Heidelberg, 2013, pp. 205–218.

[20] [Online]. Available: https://www.avl.com/fire

[21] L. T. Biegler, "An overview of simultaneous strategies for dynamic optimization," *Chemical Engineering and Processing: Process Intensification*, vol. 46, no. 11, pp. 1043 – 1053, 2007, special Issue on Process Optimization and Control in Chemical Engineering and Processing.

[22] L. T. Biegler, "Nonlinear programming strategies for dynamic chemical process optimization," *Theoretical Foundations of Chemical Engineering*, vol. 48, no. 5, pp. 541–554, Sep 2014.

[23] S. Dunker, *Tether and Bridle Line Drag in Airborne Wind Energy Applications.* Springer Singapore, 2018, pp. 29–56.

View publication stats